Supplement of
Characterisation of hygroscopic aerosol processes using remote sensing and in situ techniques at the MeteoSwiss Payerne station

Arlett Díaz-Zurita et al.

Correspondence: Francisco Navas-Guzmán (fguzman@ugr.es)

S1 Analysis of five-day NOAA HYSPLIT backward trajectories

To assess potential changes in air-mass origin with altitude, five-day (120 h) backward trajectories arriving over Payerne were calculated for each investigated hygroscopic aerosol layer using the Hybrid Single-Particle Lagrangian Integrated Trajectory (HYSPLIT) model (version 5.4.0). The trajectories were initiated at the time of the corresponding RALMO observation and at two heights corresponding to the lower and upper boundaries of each layer. For each case, the same-time separation and spatial proximity were calculated using the Haversine distance (Sinnott, 1984). The same-time separation represents the median horizontal distance between the base and top trajectories at the same backward time (e.g., base and top positions at -12 h). In contrast, the spatial proximity accounts for differences in the progression along the trajectories by determining the nearest spatial distance between the two paths, independently of backward time. This calculation was performed in both directions (base-to-top and top-to-base), and the larger of the two median distances was used as the spatial-proximity metric. A direct comparison between these metrics is shown in Fig. S1, where each point represents one investigated hygroscopic aerosol layer. The horizontal and vertical bars indicate the corresponding half interquartile range ($\pm$ IQR/2).

The results from Fig. S1 suggest that the air masses arriving at different heights within each investigated hygroscopic aerosol layer over Payerne generally follow similar paths during the first 72 h, as indicated by the relatively small same-time separation and spatial proximity values (Fig. S1a). At longer backward times (72–120 h), larger values and greater dispersion are observed (Fig. S1b). This increasing divergence may be partly related to the increasing uncertainty of numerically calculated backward trajectories with integration time (Stohl, 1998). It should also be considered that an air mass represents a horizontally extensive body of air rather than an individual trajectory (American Meteorological Society, 2000); therefore, spatial separation between individual trajectories may not indicate a change in air-mass origin. All HYSPLIT trajectory files and their corresponding maps are now available from Zenodo (https://doi.org/10.5281/zenodo.23010868; Díaz-Zurita et al., 2026).

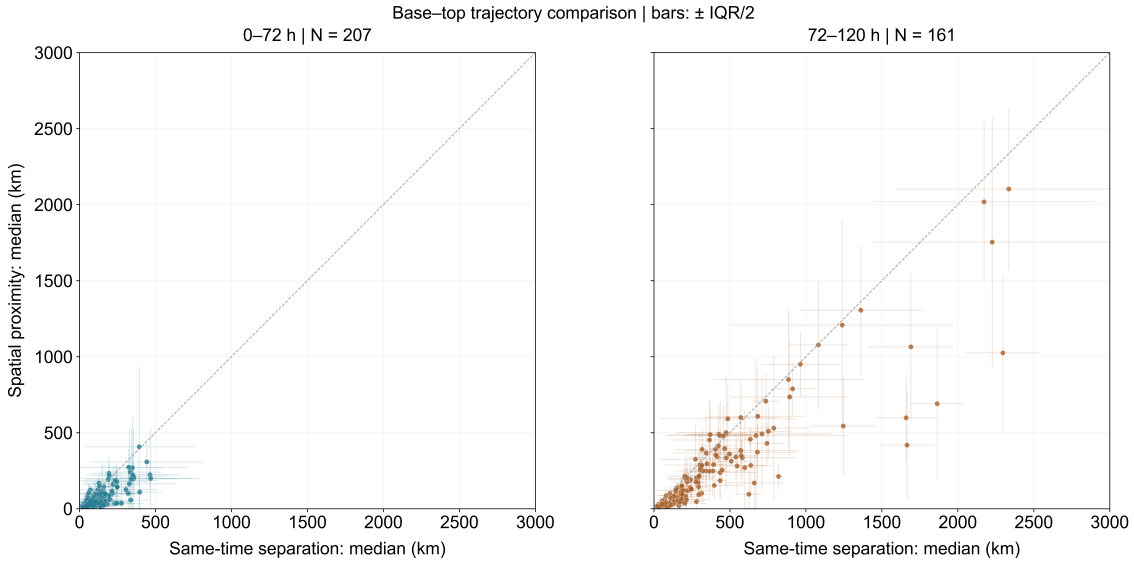


Figure S1. Comparison of five-day NOAA HYSPLIT backward trajectories for the base and top of each investigated hygroscopic aerosol layer during (a) 0–72 h and (b) 72–120 h backward time.

The five-day HYSPLIT backward trajectories for the three case studies discussed in the main manuscript are shown in Fig. S2. For each case, the analysis shows that the air masses arriving at different heights within the hygroscopic aerosol layer generally follow similar paths.

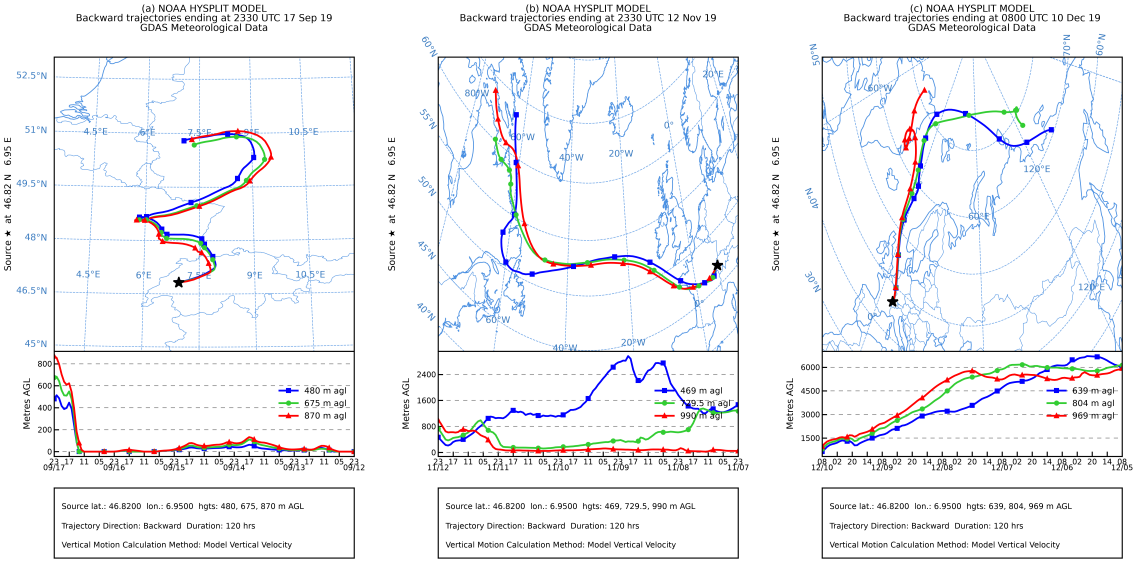


Figure S2. Five-day backward trajectories from the NOAA HYSPLIT model for (a) Case I, ending at 23:30 UTC on 17 September 2019; (b) Case II, ending at 23:30 UTC on 12 November 2019; and (c) Case III, ending at 08:00 UTC on 10 December 2019.

S2 Relationship between aerosol particle size and hygroscopicity

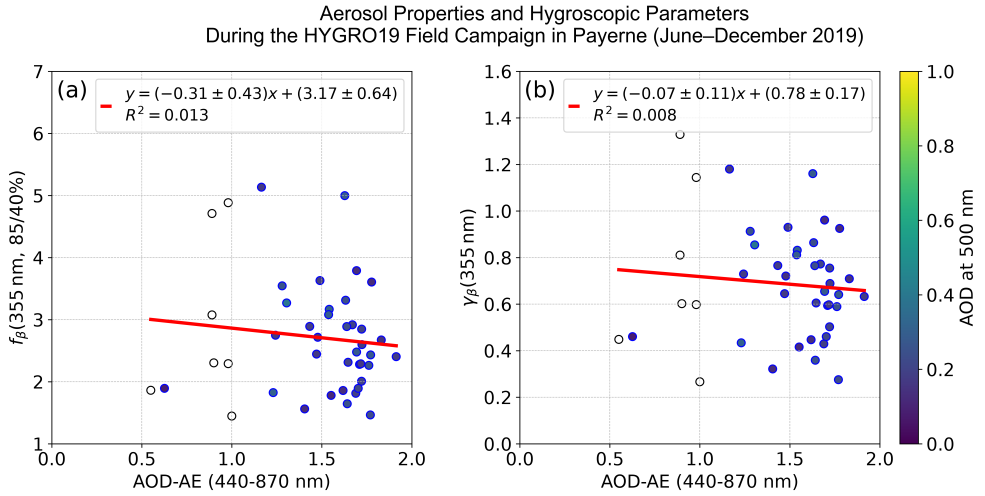


Figure S3. Relationship between the extinction Ångström exponent (AOD-AE, 440–870 nm) and the hygroscopic parameters (a) $f_\beta(355\ \mathrm{nm},\ 85/40\ \%)$ and (b) $\gamma_\beta(355\ \mathrm{nm})$ during the HYGRO19 campaign. The colour scale represents the Aerosol Optical Depth (AOD) at 500 nm. Red lines represent the linear regressions, with the corresponding equations and coefficients of determination (R^2) shown in each panel. White markers indicate cases for which no AOD measurements were available.

S3 Mie simulations of aerosol hygroscopicity

Table S1. Complex refractive indices of the dry aerosol components and water used as input in the Mie simulations.

Chemical component	355 nm	455 nm	550 nm	Reference
$(NH_4)_2SO_4$	$1.507 + 0.005i$	$1.534 + 0.000i$	$1.530 + 0.000i$	Flores et al. (2012); Beelen et al. (2014)
NH_4NO_3	$1.576 + 0.000i$	$1.559 + 0.000i$	$1.554 + 0.000i$	Beelen et al. (2014)
Organic matter	$1.550 + 0.001i$	$1.569 + 0.014i$	$1.561 + 0.010i$	Chen and Bond (2010); Beelen et al. (2014); Chang et al. (2021)
Black carbon	$1.950 + 0.790i$	$1.950 + 0.790i$	$1.950 + 0.790i$	Bond and Bergstrom (2006)
Water, H_2O	$1.343 + 0.000i$	$1.337 + 0.000i$	$1.335 + 0.000i$	Hale and Querry (1973); Chang et al. (2021)

The complex refractive index is expressed as $m = n + ik$, where n and k are the real and imaginary parts, respectively.

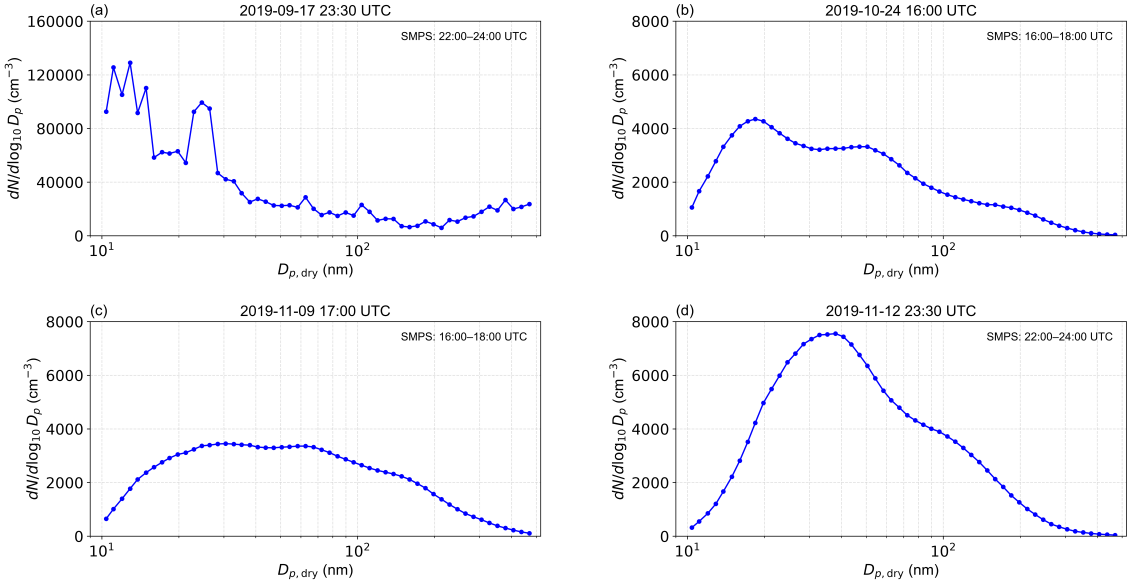


Figure S4. Aerosol size distributions measured by the SMPS and used as input for the Mie simulations, corresponding to the mean between (a) 22:00–24:00 UTC on 17 September, (b) 16:00–18:00 UTC on 24 October, (c) 16:00–18:00 UTC on 9 November, and (d) 22:00–24:00 UTC on 12 November 2019.

S4 Analysis of HYSPLIT backward trajectories and NASA/NOAA fire hotspots

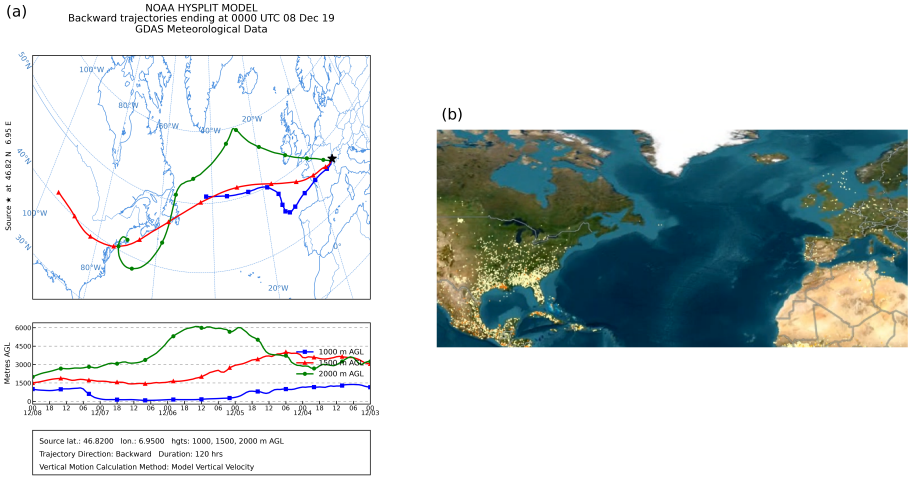


Figure S5. (a) Five-day backward trajectories from the NOAA HYSPLIT model ending at 00:00 UTC on 8 December 2019 at 1000, 1500, and 2000 m agl over Payerne. (b) Fire hotspot map from the NASA/NOAA Suomi National Polar-orbiting Partnership for the period from 4 to 8 December 2019 (https://firms.modaps.eosdis.nasa.gov/, last access: 29 September 2026).

S5 Additional observations for the intercomparisons with COBALD-RS41 sondes I: 17 September 2019

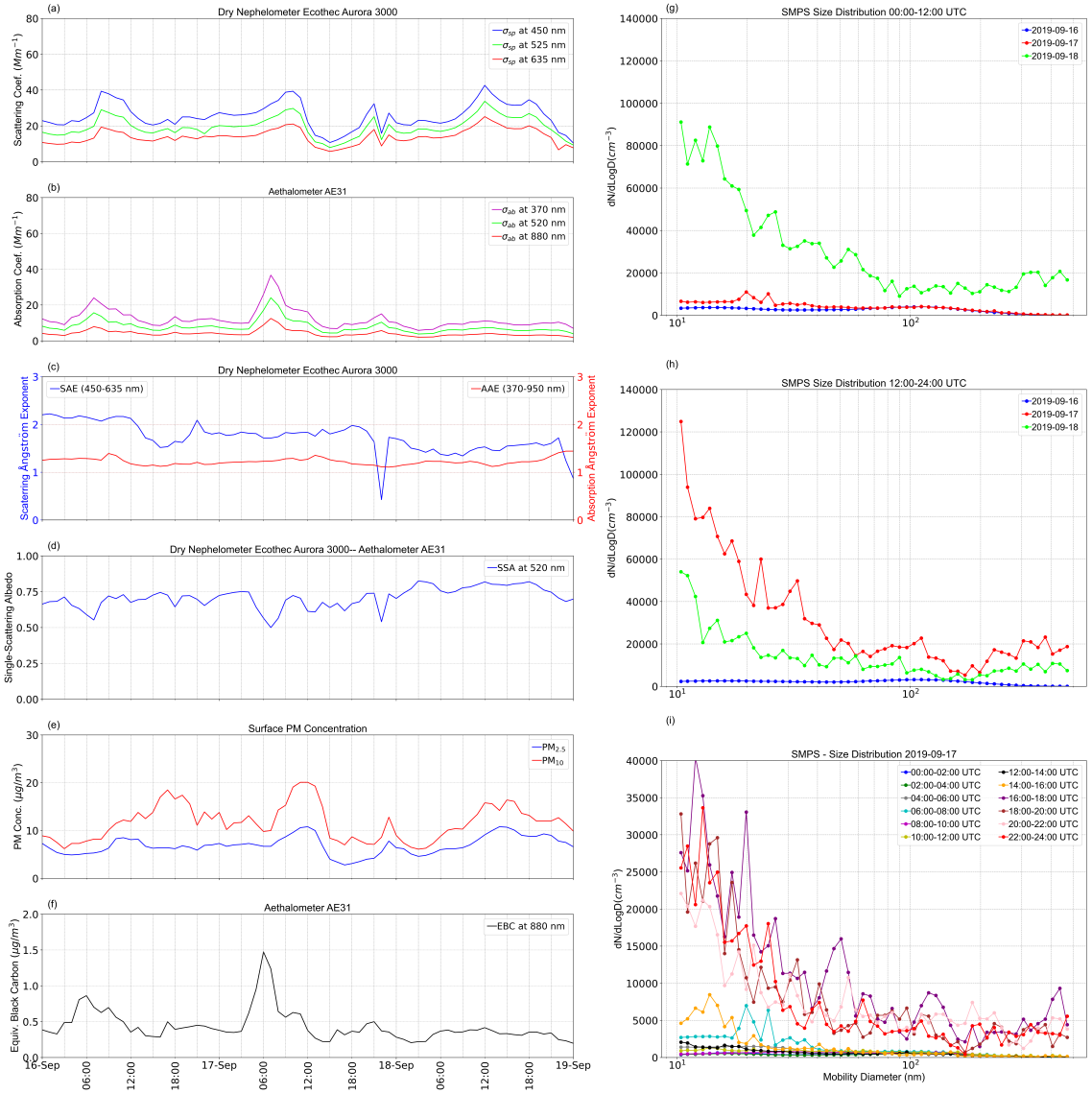


Figure S6. Time hourly series (left panels) over 16 to 18 September 2019 of: (a) aerosol scattering coefficient at 450, 525, and 635 nm from the Aurora 3000 dry nephelometer, (b) absorption coefficient at 370, 520 and 880 nm from the aethalometer AE31, (c) scattering (SAE (450–635 nm)) and absorption (AAE (370–950 nm)) *Ångström* exponents and (d) single scattering albedo (SSA) at 520 nm derived from the dry nephelometer and aethalometer, (e) PM concentrations, (f) equivalent black carbon at 880 nm from the aethalometer. Aerosol size distribution from the SMPS (right panels) for mean between (g) 00:00-12:00 UTC and (h) 12:00-24:00 UTC from 16 to 18 September 2019, and (i) 2 hourly mean on 17 September 2019.

S6 Additional observations for the intercomparisons with COBALD-RS41 sondes II and aerosol hygroscopicity near clouds: 12 November 2019

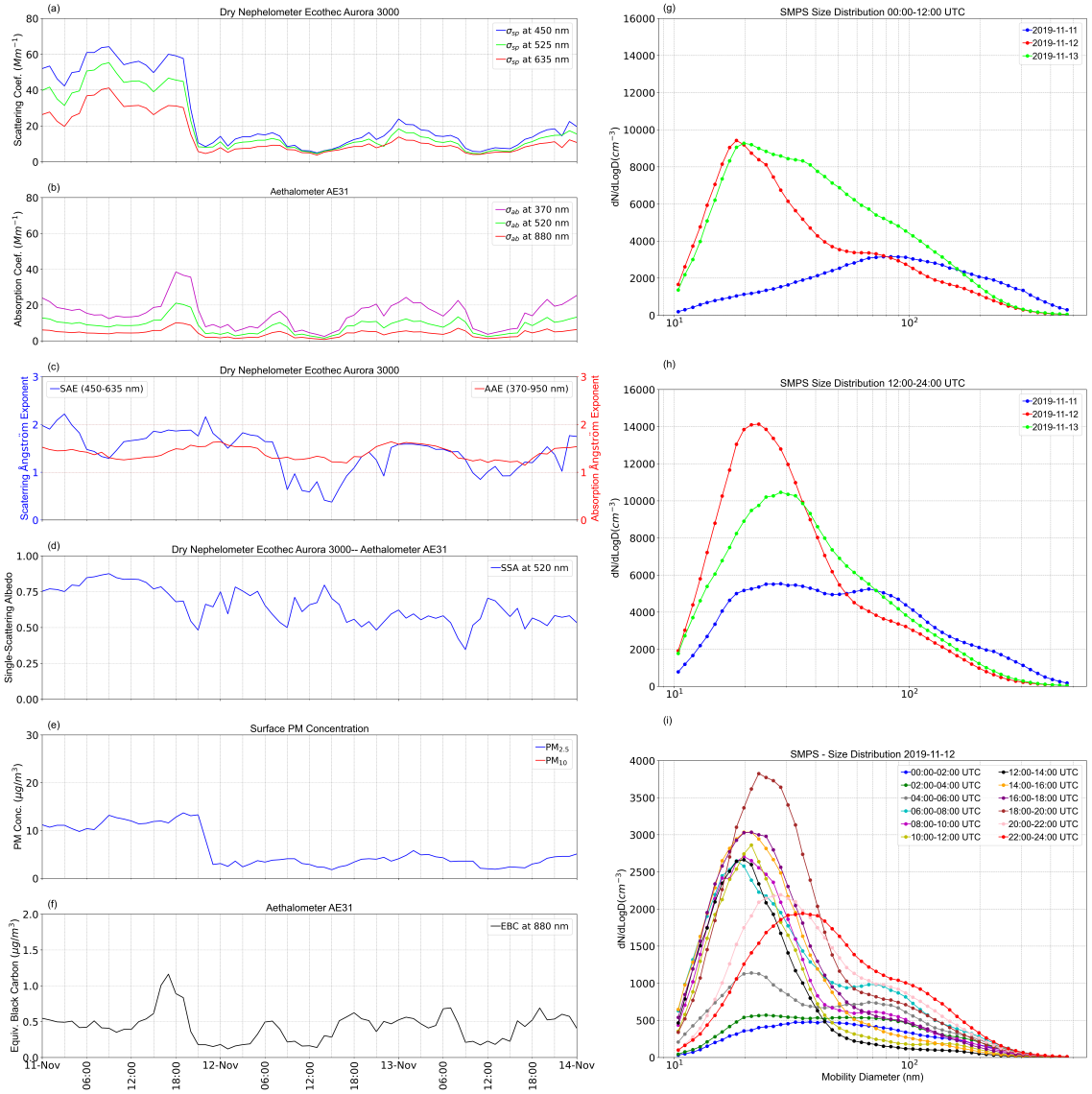


Figure S7. Time hourly series (left panels) over 11 to 13 November 2019 of: (a) aerosol scattering coefficient at 450, 525, and 635 nm from the Aurora 3000 dry nephelometer, (b) absorption coefficient at 370, 520 and 880 nm from the aethalometer AE31, (c) scattering (SAE (450–635 nm)) and absorption (AAE (370–950 nm)) *Å*ngström exponents and (d) single scattering albedo (SSA) at 520 nm derived from the dry nephelometer and aethalometer, (e) PM concentrations, (f) equivalent black carbon at 880 nm from the aethalometer. Aerosol size distribution from the SMPS (right panels) for mean between (g) 00:00-12:00 UTC and (h) 12:00-24:00 UTC from 11 to 13 November 2019, and (i) 2 hourly mean on 12 November 2019.

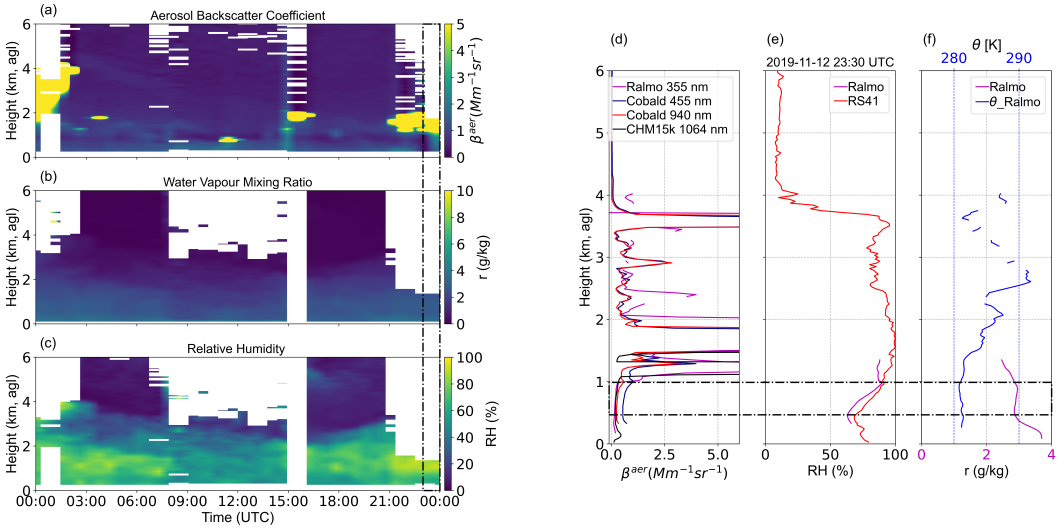


Figure S8. Temporal evolution of (a) $\beta^{aer}(355\ \mathrm{nm})$, (b) water vapour mixing ratio, and (c) RH profiles from RALMO on 12 November 2019. (d) β^{aer} profiles from RALMO at 355 nm (purple), COBALD at 455 and 940 nm (blue and red), and ceilometer at 1064 nm (black). (e) RH profiles from RALMO (purple) and RS41 (red). (f) Water vapour mixing ratio (purple) and potential temperature (blue) profiles from RALMO. The vertical profiles correspond to 23:30–23:59 UTC for RALMO and ceilometer, and 23:00–23:30 UTC for COBALD-RS41.

S7 Additional observations for aerosol hygroscopicity and clouds: 10 December 2019

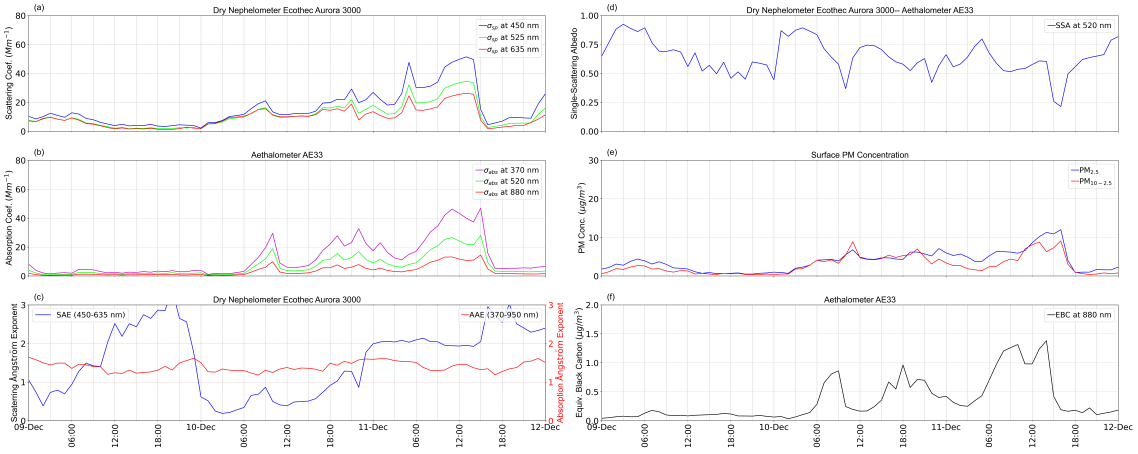


Figure S9. Time hourly series over 9 to 11 December 2019 of: (a) aerosol scattering coefficient at 450, 525, and 635 nm from the Aurora 3000 dry nephelometer, (b) absorption coefficient at 370, 520 and 880 nm from the aethalometer AE31, (c) scattering (SAE (450–635 nm)) and absorption (AAE (370–950 nm)) Ångström exponents and (d) single scattering albedo (SSA) at 520 nm derived from the dry nephelometer and aethalometer, (e) PM concentrations, (f) equivalent black carbon at 880 nm from the aethalometer.

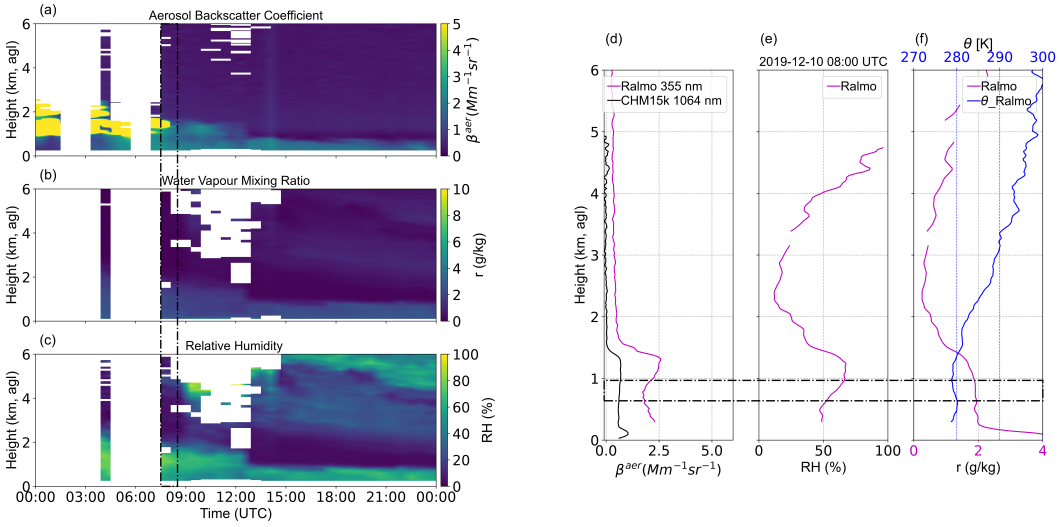


Figure S10. Temporal and vertical evolution of (a) $\beta^{aer}(355\ \mathrm{nm})$, (b) water vapour mixing ratio, and (c) RH from RALMO on 10 December 2019. (d) β^{aer} profiles from RALMO at 355 nm (purple), and ceilometer at 1064 nm (black). (e) RH, (f) Water vapour mixing ratio (purple) and potential temperature (blue) profiles from RALMO during the 08:00–08:30 UTC interval.

References

American Meteorological Society: Air mass, Glossary of Meteorology, https://glossary.ametsoc.org/wiki/air-mass/, accessed: 27 September 2026, 2000.

Beelen, A. J. V., Roelofs, G. J., Hasekamp, O. P., Henzing, J. S., and Röckmann, T.: Estimation of aerosol water and chemical composition from AERONET Sun-sky radiometer measurements at Cabauw, the Netherlands, Atmos Chem Phys, 14, https://doi.org/10.5194/acp-14-5969-2014, 2014.

Bond, T. C. and Bergstrom, R. W.: Light absorption by carbonaceous particles: An investigative review, https://doi.org/10.1080/02786820500421521, 2006.

Chang, W., Zhang, Y., Li, Z., Chen, J., and Li, K.: Improving the sectional Model for Simulating Aerosol Interactions and Chemistry (MOSAIC) aerosols of the Weather Research and Forecasting-Chemistry (WRF-Chem) model with the revised Gridpoint Statistical Interpolation system and multi-wavelength aerosol optical measurements: The dust aerosol observation campaign at Kashi, near the Taklimakan Desert, northwestern China, Atmos Chem Phys, 21, https://doi.org/10.5194/acp-21-4403-2021, 2021.

Chen, Y. and Bond, T. C.: Light absorption by organic carbon from wood combustion, Atmos Chem Phys, 10, https://doi.org/10.5194/acp-10-1773-2010, 2010.

Díaz-Zurita, A., Navas-Guzmán, F., and Pérez-Ramírez, D.: Five-day NOAA HYSPLIT backward trajectories for hygroscopic aerosol layers over Payerne, https://doi.org/10.5281/zenodo.23010868, 2026.

Flores, J. M., Bar-Or, R. Z., Bluvshtein, N., Abo-Riziq, A., Kostinski, A., Borrmann, S., Koren, I., Koren, I., and Rudich, Y.: Absorbing aerosols at high relative humidity: Linking hygroscopic growth to optical properties, Atmos Chem Phys, 12, https://doi.org/10.5194/acp-12-5511-2012, 2012.

Hale, G. M. and Querry, M. R.: Optical Constants of Water in the 200-nm to 200-μm Wavelength Region, Appl Opt, 12, 555–563, https://doi.org/10.1364/AO.12.000555, 1973.

Sinnott, R. W.: Virtues of the Haversine, Sky & Telescope, 68, 159, 1984.

Stohl, A.: Computation, accuracy and applications of trajectories - A review and bibliography, Atmos Environ, 32, https://doi.org/10.1016/S1352-2310(97)00457-3, 1998.